

## Processes controlling a volcanoclastic turbiditic system during the last climatic cycle: Example of the Cilaos deep-sea fan, offshore La Réunion Island

Emmanuelle Sisavath<sup>a, b, \*</sup>, Aude Mazuel<sup>c</sup>, Stephan J. Jorry<sup>b</sup>, Nathalie Babonneau<sup>c</sup>, Patrick Bachèlery<sup>d</sup>, Béatrice de Voogd<sup>e</sup>, Marie Salpin<sup>f</sup>, Laurent Emmanuel<sup>f</sup>, Luc Beaufort<sup>g</sup>, Samuel Toucanne<sup>b</sup>

<sup>a</sup> Laboratoire GéoSciences Réunion, Université de la Réunion, Institut de Physique du Globe de Paris, Sorbonne Paris-Cité, CNRS, UMR7154, 15 avenue René Cassin, BP 7151. 97715 Saint Denis messag Cedex 9, La Réunion, France

<sup>b</sup> IFREMER, Géosciences Marines, Laboratoire Environnements Sédimentaires, BP70, 29280 Plouzané, France

<sup>c</sup> UMR6538 Domaines Océaniques, IUEM, Université de Brest, Place Copernic, 29200 Plouzané, France

<sup>d</sup> Laboratoire Magmas et Volcans UMR 6524, CNRS-IRD-Université Blaise Pascal, Observatoire de Physique du Globe de Clermont-Ferrand, 5 rue Kessler 63038 Clermont-Ferrand, France

<sup>e</sup> Université de Pau et des pays de l'Adour et CNRS FR 2952, 64000 Pau, France

<sup>f</sup> Université Pierre et Marie CURIE, laboratoire Biominéralisation et Environnements Sédimentaires, ISTeP-CNRS, UMR7193, 75252 Paris Cedex 05, France

<sup>g</sup> CNRS, Aix-Marseille Univ, CEREGE, UMR6635, 13545 Aix en Provence cedex 4, France

\*: Corresponding author : Emmanuelle Sisavath, Tel.: + 33 2 29 00 85 65 ; fax: + 33 2 98 22 45 70 ; email address : [sisavath\\_emmanuelle@hotmail.fr](mailto:sisavath_emmanuelle@hotmail.fr)

### Abstract:

The present study focused on turbidite sedimentation in the Cilaos turbidite system, a volcanoclastic deep-sea fan recently recognized offshore La Réunion Island. A set of piston cores was collected in order to establish the stratigraphy of this fan and to examine the processes controlling the turbidite sedimentation off the Cilaos cirque (Piton des Neiges volcanic massif) over the last climatic cycle. Two main phases of turbidite activity were identified, during the ca 140–127 ka and 30–0 ka periods, coinciding with the two last glacial–interglacial transitions (i.e., Terminations II and I). In addition to changes in climate and eustatic sea-level, these periods coincide with a low effusive volcanic activity of the Piton des Neiges volcano. The high erosional rates identified in the Cilaos cirque during these intervals of both low effusive volcanic activity and enhanced rainfall level are probably the main driver of sediment supply to the deep-sea depositional system. These new findings also highlight the important capacity of volcanoclastic turbidite systems to record rapid paleoenvironmental changes.

**Keywords :** Turbidites ; La Réunion Island ; Indian Ocean ; Late Quaternary ; Volcanoclastic system

### 1. Introduction

Recent studies based on high-resolution stratigraphy show that past climate and sea-level changes have had a significant influence on deep ocean turbidite sedimentation at both orbital and millennial timescales. These relationship has been demonstrated over the last few years along both siliciclastic ( [Covault et al., 2007], [Jorry et al., 2008], [Toucanne et al., 2008], [Ducassou et al., 2010], [Jorry et al., 2011] and [Toucanne et al., 2012] among others) and carbonate margins (e.g., [Droxler and Schlager, 1985], [Schlager et al., 1994], [Andresen et al., 2003] and [Jorry et al., 2010]). Surprisingly, few studies have yet addressed the timing of gravity deposits around volcanic islands, and the forcing factors controlling the sediment delivery in such situations remain unclear ( [Alibés et al., 1999] and [Frenz et al., 2009]).

52 The conventional sequence stratigraphy model for clastic systems states that deep marine  
53 systems preferably grow during falls in sea-level and at lowstand. However, several studies  
54 have demonstrated that some turbidite systems do not follow the classic sequence stratigraphy  
55 concepts. Covault and Graham (2010) showed that deep-sea deposition occurs at all sea-level  
56 states. Terrigenous sediment delivery to the deep-sea depends on many factors, such as the  
57 tectono-morphologic character of the margin, climatic forcing and terrestrial sediment source.  
58 The influence of climate and sea-level changes on sediment delivery to volcanoclastic basins  
59 is poorly defined and remains a matter of debate. Quidelleur et al. (2008) and McMurtry et al.  
60 (2004) suggested that most large volume landslides affecting volcanic islands occur at glacial-  
61 interglacial transitions (Terminations) and concluded there was a causal relationship between  
62 flank collapses of volcanic islands and global climate change. However, recent data contradict  
63 these results, as these showed no link between climate-driven changes and volcanic flank  
64 collapses (Harris et al., 2011; Longpré et al., 2011; Rodriguez-Gonzales et al., 2009). In  
65 contrast, the influence of volcanic activity has been widely examined, especially off the  
66 Canary Islands. In this area, the main turbidite activity has coincided with phases of high  
67 volcanic activity (Schmincke and Sumita, 1998; Schneider et al., 1998).

68 Since 2006, several oceanographic cruises have been conducted on the submarine flanks of La  
69 Réunion Island (Indian Ocean). These cruises led to the discovery of five volcanoclastic deep-  
70 sea fans linked to major erosional structures visible on land (Saint-Ange et al., 2011; Sisavath  
71 et al., 2011). La Réunion Island offers the opportunity to study a deep depositional system  
72 related to an isolated oceanic island, situated far from continental influences. The aim of this  
73 paper is to establish the first stratigraphy of the Cilaos turbidite system based on a set of  
74 Küllenberg piston cores. We discuss how volcanic activity, climate and sea-level variations  
75 have interacted and controlled the input of sediment offshore of La Réunion island over the

76 last 140 ka, leading to the building of a deep-sea fan spreading over hundreds of kilometers  
77 on the sea floor.

78

## 79 **2. Physical setting**

80

### 81 *2.1. General setting of La Réunion Island*

82

83 La Réunion Island is an isolated volcanic system located 750 km from Madagascar in the  
84 western part of the Indian Ocean (Fig. 1). It belongs to the Mascarene Archipelago and  
85 resulted from the activity of the hotspot that formed the Deccan Trapps (65 Ma ago) and  
86 subsequently the Mascarene Plateau and Mauritius Island (Bonneville et al., 1988; Duncan et  
87 al., 1989; Morgan, 1981). It is the youngest and largest island in this group and the only one  
88 that has active volcanism today. The island is located on an isolated compartment of the  
89 oceanic crust (~67 Ma) bordered by two fracture zones (FZ) separated by 350 km: the  
90 Mahanoro FZ to the west and Mauritius FZ to the east (Fig. 1).

91 La Réunion Island s.s. is the emerged part of a volcanic edifice rising from approximately -  
92 4200 m (the oceanic floor) to more than 3000 m above sea level. The subaerial island  
93 represents only three percent of the whole edifice (De Voogd et al., 1999). The submarine  
94 flanks of La Réunion Island are mostly built by accumulation of debris avalanche deposits  
95 (Lénat and Labazuy, 1990; Oehler et al., 2004). In the southwestern part of the island, no  
96 major failures or flank collapses have produced deposits for 1 Ma (Oehler et al., 2008).

97 The island is elliptical in shape (50 × 70 km) and composed of two basaltic shield-volcanoes:  
98 Piton des Neiges and Piton de la Fournaise (Fig. 1). Activity of Piton de la Fournaise (2632  
99 m high) started less than 0.6 Ma ago and this volcano is still highly active (Gillot and Nativel,  
100 1989). Its morphology is marked by a succession of calderas open to the sea on their eastern

101 sides (Fig. 1). The historic volcanic activity of Piton de la Fournaise has been described by  
102 Bachelery et al. (1983), Lenat et al. (2009), Michon and Saint-Ange (2008), Peltier et al.  
103 (2009; 2008) and Stieltjes et al. (1988).

104 The Piton des Neiges volcano (3070 m high) occupies the northwestern two thirds of the  
105 island. The principal and most original feature of this volcano is the existence of three major  
106 erosional depressions, called “cirques”, opened in the heart of the volcano (Fig. 1). The  
107 cirques were partly filled by unconsolidated detrital rocks such as volcanic debris, avalanche  
108 deposits, debris flow deposits and other breccia (Arnaud, 2005; Bret et al., 2003; Fèvre, 2005;  
109 Oehler et al., 2005). Piton des Neiges started to grow more than 2.17 Ma ago, and has been  
110 inactive for at least 0.012 Ma (Deniel et al., 1992; McDougall, 1971; Quidelleur et al., 2010;  
111 Smietana et al., 2010). Its subaerial shield-building stage, known as the Oceanite Series,  
112 extended from 2 Ma to approximately 430 ka (Deniel et al., 1992; McDougall, 1971; Upton  
113 and Wadsworth, 1965). The second stage, known as the Differentiated Series, occurred  
114 between 350 and 12 ka (Deniel et al., 1992; Gillot and Nativel, 1982; McDougall, 1971), with  
115 the end of the main effusive activity at about 30 ka (Gillot and Nativel, 1982). The second  
116 stage can be divided into three sub-stages. The first, between 350 and 180 ka, corresponded to  
117 the beginning of Piton des Neiges magmatic differentiation. This effusive activity produced  
118 lava flows that covered most of the edifice, filling existing valleys (Gillot and Nativel, 1982).  
119 The second sub-stage corresponded to a low effusive activity period lasting 40 ka (Kluska,  
120 1997), with mainly explosive activity (Kieffer, 1990). Kluska (1997) suggested that this was a  
121 major erosional period corresponding to the formation of large and deep depressions: the  
122 cirques. A second period of effusive activity took place between 140 and 30 ka.

123

124 *2.2. Local climate*

125

126 La Réunion Island is located in the subtropical zone, where it is influenced by the South  
127 Equatorial Current and subjected to a prevailing southeasterly trade-wind regime. Trade  
128 winds from the east induce highly variable precipitation regimes in time and space, which  
129 lead to the island having a wet windward side (East) and a dry leeward side (West). Rainfall  
130 also varies according to the elevation (dry coast - wetter upland), with maximum rain in the  
131 mid-slope area. Average annual rainfall varies from over 12 000 mm per year between 1300  
132 and 2000 m altitude on windward slopes, to as low as 600 mm near the leeward coast.  
133 The late Quaternary climate of La Réunion Island is largely unknown, as no data are available  
134 for this area.

135

### 136 2.3. *Drainage basins and rivers*

137

138 On La Réunion Island, the wet tropical climate and basaltic terrains cause high erosion rates,  
139 which are amplified by seasonal cyclonic conditions (Louvat and Allegre, 1997; Rad et al.,  
140 2007). These erosion rates are close to those estimated in active orogenic areas, with values  
141 ranging between  $0.47 - 3.4 \text{ m.kyr}^{-1}$ . They result in a dense hydrographic network with more  
142 than 750 gullies and rivers on the island, concentrated in drainage basins like the cirques and  
143 the main valleys. These drainage basins are located between the planeze areas (Ollier and  
144 Terry, 1999), which are relatively unaffected by erosion because water penetrates rather than  
145 forming surface runoff (Fèvre, 2005). In the drainage basins, the rivers are torrential with  
146 mechanical erosion rates among the highest measured in the world, ranging from 1200 to  
147  $9100 \text{ t/km}^2/\text{yr}$  (Louvat and Allegre, 1997).

148 One of the major rivers of the island is the “Rivière Saint-Etienne”. It is a torrential river  
149 formed by the junction of the “Bras de Cilaos”, which drains the inner part of the Cirque of  
150 Cilaos, and the “Bras de la Plaine”, which drains the outer eastern part (Fig. 1). The Saint-

151 Etienne River has a drainage basin of about 200 km<sup>2</sup> reaching altitudes of 2500 to 3000 m. Its  
152 mean fluvial solid load is estimated around 470 000 m<sup>3</sup>/yr; up to 1-2 million m<sup>3</sup>/yr during  
153 large floods (SOGREAH, 1998). In addition to this drainage basin, the outer western part of  
154 the Cirque of Cilaos is incised by many gullies (Fig. 1). The resulting drainage basin for the  
155 Cirque of Cilaos (“Rivière Saint-Etienne” and gullies) is about 360 km<sup>2</sup>.

156 The transition between the subaerial and submarine environments is marked by a narrow  
157 shelf. The local absence of this shelf and the presence of steep submarine slopes around the  
158 island imply a rapid transfer of sediment from the coast toward the base of the volcanic  
159 edifice, allowing the formation of a volcanoclastic deep sea fan.

160

#### 161 *2.4. The Cilaos turbidite system*

162

163 Recent oceanographic cruises over the submarine flanks of La Réunion Island and the  
164 surrounding oceanic plate led to the discovery of five volcanoclastic turbidite systems (Fig. 1)  
165 extending over 200 km away from the island (Saint-Ange et al., 2011; Sisavath et al., 2011).  
166 On land, these systems are related to major erosional features that constitute the main  
167 drainage area of the island. In each case, submarine canyons are directly connected to the  
168 main river mouths. The Mafate fan is connected to the Cirque of Mafate, and the Saint-Joseph  
169 fan is the only system connected to the Piton de la Fournaise volcano. The latter is considered  
170 an embryonic stage fan. Finally, the Cilaos fan is the widest fan and is connected to the  
171 Cirque of Cilaos.

172 The Cilaos turbidite system is located to the southwest of La Réunion Island. It is more than  
173 250 km long and covers an area of about 15 000 km<sup>2</sup>. This sedimentary system extends from  
174 the Saint-Etienne river mouth to the Mahanoro fracture zone (Fig. 1). It starts at the coast,  
175 with a 70 km long bypass area that directly feeds a deep-sea fan developing at about 4500 m

176 water depth. The Cilaos fan extends over a complex abyssal plain composed of NE-SW  
177 volcanic ridges (Saint-Ange et al., 2011).

178 The canyon area (Fig. 1; outlined in blue) is composed of two main canyons, Saint-Etienne  
179 and Pierrefonds. The Pierrefonds canyon is located in front of the older Saint-Etienne River  
180 delta and is connected to the shelf by many tributary canyons. The Saint-Etienne canyon is 4  
181 km wide and is directly connected to the present day Saint-Etienne River. Both canyons  
182 merge into the single wide Cilaos canyon, which feeds the main deep sea fan body.

183 The fan can be divided into two parts: the proximal fan (Fig. 1; outlined in red) and distal fan  
184 (Fig. 1; outlined in yellow). The proximal fan is broad, with a maximum width of 120 km and  
185 low reflectivity of backscatter data. It is composed of elongated bodies, interpreted as small  
186 lobes. The sedimentation in the proximal fan is characterized by coarse sandy turbidites  
187 (Sisavath et al., 2011). The distal fan is divided into three parts, western, central and eastern,  
188 by pre-existing volcanic ridges. The distal prolongation of the turbidite system is visible at the  
189 ends of the western and central parts. It is characterized by elongated structures, extending via  
190 narrow channels from the proximal fan. The sediments of the distal fan are composed of a  
191 succession of fine sandy turbidites covered by a thick clay layer (about 3 m in thickness; Figs.  
192 2 and 3).

193

### 194 **3. Materials and Methods**

195

196 In this paper, we used seven Küllenberg piston cores taken around La Réunion Island during  
197 the oceanographic cruises ERODER 1, onboard the BHO *Beautemps-Beaupré* in 2006;  
198 FOREVER, onboard the R/V *Atalante* in 2006; and ERODER2, onboard the R/V *Meteor* in  
199 January 2008 (Fig. 1, Table 1). Five cores were taken from locations in the Cilaos fan  
200 (KERO-09, KERO-16, KERO-12, KERO-15 and FOR-C1). Additional cores from the Mafate

201 fan (KERO-07, Fig. 1) and the Saint-Joseph fan (KERO-08, Fig. 1) were used to build a  
202 regional age model. All the cores were situated and correlated using Parasound and 3.5 kHz  
203 echosounder profiles acquired during the FOREVER and ERODER2 cruises (Fig. 3).  
204 Sedimentary descriptions were made of all the cores, with a particular emphasis on sediment  
205 color, visual grain size and turbidite/hemipelagite/pelagite differentiation. Two main types of  
206 sediment were distinguished: volcanoclastic sandy turbidites and hemipelagic sediments.

207 A series of 1-cm-thick sediment slabs were collected from each split core section and  
208 examined by X-radiography using a SCOPIX digital X-ray imaging system (Migeon et al.,  
209 1999). Digital images were acquired to provide a precise identification of the sedimentary  
210 structures. Sediment cores were sampled for grain-size analyses using a Coulter laser micro-  
211 granulometer (LS130). The variation of Ca through each of the cores was measured with an  
212 Avaatech XRF Core-Scanner equipped with a variable optical system allowing measurements  
213 at resolutions between 10 and 0.1 mm. The selected measurement area was 8 mm and the  
214 step-size was set at 1 cm.

215 Oxygen isotope analyses were conducted on small batches of *Globigerinoides ruber*, the  
216 monospecific planktonic foraminifer that calcifies in the surface mixed layer, from cores  
217 KERO-07, KERO-08, KERO-09 and KERO-16. Samples were collected at hemipelagic  
218 intervals, representing intervals of continuous sedimentation, excluding turbidites. Cores were  
219 sub-sampled with a sample spacing of 5 to 20 cm. On average, 15 specimens were picked out  
220 from the >150  $\mu\text{m}$  fraction. Using a common 100% phosphoric acid bath at 90°C, 20–50  $\mu\text{g}$   
221 of sample were reacted and analyzed using a GV Isoprime isotope ratio mass spectrometer at  
222 University of Pierre & Marie Curie (Paris). Isotope values are given in delta notation relative  
223 to Vienna Peedee belemnite. Repeated analyses of a marble working standard (calibrated  
224 against the international standard NBS-19) indicate an accuracy and precision of 0.1‰ (1 $\sigma$ ).



225 In core KERO-16, the last occurrence of pink-pigmented *G. ruber* indicates the transition  
226 between Marine Isotopic Stage (MIS) 6 and MIS 5 (Thompson et al., 1979).

227 Nine AMS radiocarbon dates were obtained on the cores (Table 2). For each sample, about 10  
228 mg of *G. ruber* and *G. sacculifer* specimens were picked out from the >150 mm fraction,  
229 washed in an ultrasonic bath with distilled water, and dried. These samples were then  
230 analyzed at the Poznan Radiocarbon Lab., Poland, and at the “Laboratoire de Mesure du  
231 Carbone 14” at Saclay, France. Reported radiocarbon ages were corrected for a marine  
232 reservoir effect of 400 years and converted to calendar years using CALIB Rev 6.0 (Reimer et  
233 al., 2009). Calibrated kilo years before the present will be referred as ka.

234 The preservation of the test surface of the foraminifer *G. ruber* was examined by Scanning  
235 Electron Microscopy (SEM, Philips XL30). The analysis was performed on *G. ruber* from  
236 seven samples studied for  $\delta^{18}\text{O}$  measurements (three in core KERO-09 and four in core  
237 KERO-16). Foraminifera were placed on adhesive carbon tabs and coated with gold. The  
238 observation of the test surfaces was done in the secondary electron mode at 10 kV voltage and  
239 at a distance of 10 mm.

240 In core KERO-09, five representative samples associated with particular sedimentary facies  
241 were also analyzed for calcareous nannofossil biostratigraphy (Table 3). Smear slides were  
242 made directly from unprocessed samples and were examined with a polarized light  
243 microscope at a magnification of 1000 $\times$ .

244

## 245 **4. Results**

246

### 247 *4.1. Lithology and echosounding facies*

248

249 Based on the grain-size characteristics, internal sedimentary structures, erosive contacts with  
250 underlying sediments and the abundance of glass shards and volcanic crystals, all the sandy  
251 beds in the studied cores were interpreted as volcanoclastic turbidites (Saint-Ange et al., 2011;  
252 Sisavath et al., 2011). These turbidite units ranged from a few centimeters up to 20 cm in  
253 thickness (Fig. 2).

254 Cores KERO-09 and KERO-12, taken in the western part of the Cilaos distal fan at  
255 about 215 km from the island, were 6.27 and 6.40 m long, respectively (Fig. 1). The lower  
256 parts of these cores are characterized by a succession of four sandy units of 30 to 50 cm thick,  
257 composed of well-sorted fine sand showing typical Bouma Tb to Te sequences (Bouma,  
258 1962) (Fig. 3). On the echosounder profiles, this lowest unit corresponds to a stratified unit  
259 named U1 (Fig. 3). A thick layer of clay (about 3 m thick), showing an alternation of light  
260 brown clay and darker brown clay, overlies this unit. The light brown clay is dominated by  
261 calcareous sediment (composed of nannoplankton and foraminifera), while the dark brown  
262 clay mainly contains siliceous organisms (radiolarians and diatoms). On the echosounder  
263 profiles, it corresponds to a semi-transparent unit, named U2 (Fig. 3).

264 Core KERO-15 was taken in the most distal part of the Cilaos distal fan at about 280  
265 km from the island (Fig. 1). This 6.68 m-long core shows a sedimentary pattern similar to that  
266 observed in cores KERO-09 and KERO-12. The base of the core shows a succession of seven  
267 fine-sandy layers (20 to 80 cm thick) with typical Bouma Tb to Te sequences, and belongs to  
268 unit U1 on the echosounder profiles (Fig. 3). The upper part of the core is composed of a clay  
269 layer of about 2 m thick showing an alternation of light brown clay and darker brown clay,  
270 corresponding to the unit U2 on the echosounder profiles (Fig. 3).

271 Core KERO-16 (4.95 m) was taken at a water depth of 4340 m, in the central part of  
272 the Cilaos distal fan, on the right side of a channel. Clay layers (alternation of light brown  
273 clay and darker brown clay) dominate the lithological succession in the lower part of the core,

274 which locally includes small bioturbation features. This unit corresponds to unit U2 on the  
275 echosounder profiles. At the top of the core (0-1.4 meters below seafloor, mbsf), fine-grained  
276 turbidite deposits of few centimeters thickness are visible (Fig. 2). They were interpreted as  
277 overflow deposits. On the echosounder profiles, they correspond to the upper part of the  
278 profiles, characterized by a stratified unit named U3.

279 Core FOR-C1 was taken at the top of a sedimentary ridge in the central part of the  
280 distal fan at a water depth of 4074 m (Fig. 1). The 2.50 meters forming the base of the core  
281 are composed of an alternation of clay and thin sandy turbidites (less than 10 cm thick). This  
282 unit corresponds to the unit U1 on the echosounder profiles (Fig. 3). It is overlain by 1.50 m  
283 of clay (alternation of light brown clay and darker brown clay) corresponding to the semi-  
284 transparent unit U2 on the echosounder profiles (Fig. 3). The top 0.54 cm are composed of  
285 clay interbedded with thin sandy layers (1 cm thick), interpreted as overflow deposits and  
286 corresponding to the stratified unit U3 on the echosounder profiles (Fig. 3).

287 Core KERO-07 was taken in the Mafate fan at a water depth of 791 m. It is a 3.40 m-  
288 long core from the left side of the canyon area (Fig. 1). The lower two thirds of the core  
289 correspond to a succession of sandy and silty turbidite sequences that are variable in  
290 thickness, while the upper third is composed of silty-clay (Fig. 2).

291 Core KERO-08 was taken near the volcanic ridge R4 at a water depth of 4126 m, in  
292 the distal part of the Saint-Joseph fan. Its lithological succession is composed of a succession  
293 of sandy and silty turbidites whose thicknesses range from 2 to 15 cm. These well-sorted  
294 turbidites show normal grading and horizontal laminations. In the dark sandy layers,  
295 laminations are underlined by white laminae characterized by abundant foraminifera and  
296 bioclasts. Some clay and silty clay layers are highly bioturbated.

297

298 *4.2. Chronostratigraphic framework*

299

300 The chronostratigraphic framework of cores KERO-09, KERO-16, KERO-07 and KERO-08  
301 was established through integration of radiocarbon dating, planktonic oxygen isotope,  
302 biostratigraphic markers and XRF records.

303 The  $\delta^{18}\text{O}$  curves show similar trends between all cores (Figs 5 and 6). The upper parts of the  
304 cores show light  $\delta^{18}\text{O}$  values (down to -2.0 ‰ in core KERO-07). A rapid increase of the  $\delta^{18}\text{O}$   
305 signal is observed thereafter, and heavier  $\delta^{18}\text{O}$  values (from -1.0 to 0 ‰) characterized the  
306 lower parts of the cores (Fig. 4). Peaks and troughs recognized in the oxygen isotope records  
307 were correlated with the reference isotopic signal published by Fretzdorff et al. (2000) from  
308 La Réunion area, in agreement with the trends of the  $\delta^{18}\text{O}$  benthic stack record of Lisieky and  
309 Raymo (2005) (Figs. 4 and 5).

310 The light  $\delta^{18}\text{O}$  values observed in the upper part of the cores correspond to the Holocene (<11  
311 ka). MIS2 is characterized by values of  $\delta^{18}\text{O}$  between 0 and -0.5 ‰. A general decrease of the  
312  $\delta^{18}\text{O}$  values from 0 to -1 ‰ is clearly shown in MIS3 (Fig. 5). It is followed by an increase of  
313  $\delta^{18}\text{O}$  values identified as the MIS3/MIS4 transition. The relatively light  $\delta^{18}\text{O}$  values (>-1‰)  
314 observed in the lower part of cores from the Cilaos fan correspond to the last interglacial. The  
315 oxygen isotope stratigraphy of all these cores provides a regional record of the last climatic  
316 cycle around La Réunion Island.

317 In cores of the Cilaos fan (KERO-09 and KERO-16), MIS-5 is characterized by  $\delta^{18}\text{O}$  values  
318 ranging between -1 ‰ and 0 ‰, which are unusually low for the last interglacial compared  
319 with those published by Fretzdorff et al. (2000) (Fig. 5). SEM observations of the test surface  
320 of *G. ruber* in cores KERO-09 and KERO-16 reveal some dissolution pockets and  
321 recrystallized areas (Fig. 6), which could explain these inconsistent  $\delta^{18}\text{O}$  values. In addition,  
322 periods of high carbonate dissolution have been identified in the western part of the Indian

323 ocean, mainly during interglacials (Divakar et al., 1993). However, this chronostratigraphy  
324 was supported by the study of biostratigraphic markers. The nannofossil assemblage in core  
325 KERO-09 contains abundant *E. huxleyi* at 65 cm below seafloor (bsf), suggesting an age  
326 younger than 75-90 ka (Berggren et al., 1995). Samples from 115-117 and 361 cm bsf show  
327 abundant well preserved nannofossils. The occurrence of *E. huxleyi* and the absence of *P.*  
328 *lacunosa* suggest that these samples are younger than 260 ka (Berggren et al., 1995). The  
329 sample from 608 cm bsf has abundant but a poorly preserved nannofossils. *Gephyrocapsa spp*  
330 *cf caribbeanica* is dominant and two *P. lacunosa* are present, suggesting an age younger than  
331 460 ka (Berggren et al., 1995). The last occurrence of pink pigmented *G. ruber* is also  
332 observed in core KERO-16 at 4.70 m bsf, suggesting that the upper 4.70 m of KERO-16 is  
333 aged 120 ka (Thompson et al., 1979).

334 All these data provide a consistent age model around La Réunion Island. This age model was  
335 extended to other cores of the Cilaos fan (KERO-12, KERO-15 and FOR-C1) using the XRF  
336 records. The age model of cores FOR-C1, KERO-12 and KERO-15 was established by  
337 correlating the Ca variation of cores KERO-09 and KERO-16 (Fig. 7). In all the cores, light  
338 brown clays, corresponding to high XRF Ca values, allow a reliable core-to-core correlation.

339

#### 340 4.3. Lithostratigraphy

341

342 The lithostratigraphy in the Cilaos fan was established with cores KERO-09, KERO-12,  
343 KERO-15, KERO-16 and FOR-C1. Based on the age model, the five cores retrieved from the  
344 Cilaos fan extend from 10 ka to 130 ka, with the Holocene period only being recorded for  
345 KERO-16 (Fig. 4). Although distances of tens of kilometers separate them, the variation of  
346 the calcium XRF correlates well between the five cores through the last glacial-interglacial  
347 cycle (Fig. 7). The cores exhibit a common sediment pattern and a fairly similar

348 sedimentation rate. They are all composed of a succession of turbidites covered by a thick  
349 clay layer (Fig. 2). The sedimentation rate in the hemipelagic layer ranges between 1.8 and  
350 5.2 cm/ka (Fig. 8). These results are comparable to the minimum sedimentation rate of 1.9  
351 cm/ka observed by Ollier et al. (1998), based on micropaleontological analysis. They also  
352 correlate with the sedimentation rates measured by Fretzdorff et al. (2000) in core S 17-666,  
353 near the Mafate fan (Fig. 1), based on a  $\delta^{18}\text{O}$  stratigraphy (Fig. 4). In this core (S17-666),  
354 three stages can be observed in the sedimentation: 1) between 128 and 186 ka, with a  
355 sedimentation rate of 4.14 cm/ka; 2) between 26 and 128 ka, with an average rate of  
356 sedimentation of 2.27 cm/ka; and 3) between 14.5 and 26 ka, with a sedimentation rate of  
357 4.35 cm/ka. If we calculate the mean of the sedimentation rates in our cores for each period,  
358 we obtain sedimentation rates of about 4.9 cm/ka for the first stage, 2.73 cm/ka for the second  
359 stage and 3.02 cm/ka for the third. The sedimentation rates lie between those of the Mafate  
360 and Cilaos systems, with two stages of relatively high sedimentation rate interrupted by a  
361 period of low sedimentation.

362 These three distinct phases of sedimentation correlate with the three sedimentary units  
363 identified in the cores of the Cilaos turbidite system. The first unit corresponds to the turbidite  
364 activity visible in the lower part of cores KERO-09, KERO-12 KERO-15 and FOR-C1,  
365 characterized by sandy turbidites of 30 to 50 cm thickness (Fig. 3) and corresponding to the  
366 stratified unit U1 on the echosounder profiles (Fig. 3). This first stage is characterized by  
367 turbidity currents that spread over the entire fan (Sisavath et al., 2011). This first documented  
368 phase of turbidite activity would have deposited until the end of MIS5 (Fig. 8). Therefore,  
369 according to the age model of figure 8, the top of unit U1 – marking the interruption of this  
370 first phase of turbidite activity – corresponds to an age of 125-127 ka.

371 The second phase is characterized by a thick clay layer observed in all the cores (Fig. 2) and  
372 by the absence of major turbidite activity. Only a few thin sandy layers are observed in cores

373 FOR-C1 and KERO-16 (Fig. 8). On the echosounder profiles, this unit coincides with the  
374 semi transparent unit U2, visible over the entire fan except in the more proximal part  
375 (Sisavath et al., 2011). The timing of clay deposition ranged from MIS3 to MIS5 (Fig. 8). The  
376 top of unit U2, visible in the upper part of cores KERO-16 and FOR-C1, lies within the lower  
377 part of MIS2 at about 30 ka (Fig. 8).

378 The third phase is characterized by thin sandy layers observed in cores FOR-C1 and KERO-  
379 16 (Fig. 3), with sediments coarser than in the older phase of turbidite activity. These turbidite  
380 events were observed on the proximal fan and into the channels of the distal fan (Sisavath et  
381 al., 2011). They are characterized, on the echosounder profiles, by a stratified unit (U3)  
382 visible in the upper part of the profiles (Fig. 3). This phase corresponds to the most recent  
383 activity of the Cilaos fan and was deposited during MIS1 and MIS2 until 30 ka.

384

## 385 **5. Discussion**

386

387 This discussion is based on cores KERO-09, KERO-12, KERO-15, KERO-16 and FOR-C1.  
388 Cores KERO-07 and KERO-08 were used to build a consistent regional  $\delta^{18}\text{O}$  stratigraphy  
389 around La Réunion Island.

390

### 391 5.1. Sedimentation in the Cilaos fan over the last 140 ka

392

393 Three distinct episodes of sedimentation correlate with three sedimentary units identified in  
394 the cores of the Cilaos turbidite system. The first unit corresponds to the oldest turbidite  
395 activity, visible in the lower part of cores KERO-09, KERO-12 KERO-15 and FOR-C1. This  
396 first unit, spreading over the entire fan (Sisavath et al., 2011), is characterized by sandy  
397 turbidites of 30 to 50 cm thick (Fig. 3) and corresponds to the stratified unit U1 on the

398 echosounder profiles (Fig. 3). According to our age model (Fig. 8), the first period of turbidite  
399 activity began before 140 ka and ended at  $\sim$  125-127 ka (which coincides with the MIS5  
400 highstand).

401 The second phase is characterized by a thick clay layer observed in all the cores (Fig. 2)  
402 which illustrates the absence of major turbidite activity. Only a few thin sandy layers are  
403 observed in cores FOR-C1 and KERO-16 (Fig. 8). On the echosounder profiles, this unit  
404 coincides with the semi transparent unit U2, visible over the entire fan except in the more  
405 proximal part (Sisavath et al., 2011). The timing of clay deposition ranged from MIS3 to  
406 MIS5 (Fig. 8). The top of unit U2, visible in the upper part of cores KERO-16 and FOR-C1,  
407 lies within the lower part of MIS2 at about 30 ka (Fig. 8).

408 The third phase is marked by the deposition of thin sandy layers as observed in cores FOR-C1  
409 and KERO-16 (Fig. 3), with sediments coarser than those deposited during the older U1 unit.  
410 These turbidite events were active in the proximal fan and into the channels of the distal fan  
411 (Sisavath et al., 2011). They are characterized, on the echosounder profiles, by a stratified unit  
412 (U3) visible in the upper part of the profiles (Fig. 3). This phase corresponds to the most  
413 recent activity of the Cilaos turbiditic fan since 30 ka until Holocene.

414 A significant difference in sedimentation rate is observed between core KERO-16 (located  
415 near the main channel of the central part of the Cilaos fan, showing the highest sedimentation  
416 rate) and the other cores KERO-09, KERO-15, KERO-12 and FOR-C1 (Fig. 9). The location  
417 of cores KERO-09, KERO-15 and KERO-12 at the termination of the distal fan might explain  
418 a lower sediment supply compared to the upper/central part of the Cilaos fan. The location of  
419 core FOR-C1 on top of a sedimentary ridge (about 200 m-high) explain sedimentation rates  
420 significantly lower than those observed in KERO-16.

421 In the distal part of the Cilaos fan, sedimentation rate is rather homogeneous until  $\sim$  60 ka and  
422 decreases from  $\sim$  60 ka to  $\sim$  10 ka (Fig. 9), which corresponds to the progressive abandon of



423 the turbiditic sedimentation in the western distal part of the Cilaos fan since ~ 60 ka (Sisavath  
424 et al., 2011). The increase of sedimentation rate from ~ 100 ka to ~ 45 ka in cores KERO-16  
425 and FOR-C1 reflects a turbiditic activity restricted to the central part of the fan.  
426 From ~ 45 ka to ~ 30 ka, decrease in sedimentation rates in all cores can be interpreted as a  
427 major change in the sediment supply at the scale of the entire Cilaos deep-sea fan (Fig. 9).  
428 This period coincides with the youngest phase of effusive volcanic activity of the Piton des  
429 Neiges (Kluska, 1997, Salvany et al., 2012), which has probably contributed to fill the cirques  
430 and the fluvial valleys. At ~ 30 ka, the major increase in sedimentation rates detected in core  
431 KERO-16 corresponds to a new episode of turbidite activity (unit U3, Fig.9) restricted to the  
432 central part of the fan (Sisavath et al., 2011).

433

434 5.2. Unravelling the forcing factors of turbidite sedimentation in the Cilaos fan over the last  
435 140 ka

436

437 The three main forcing factors controlling sediment supply and transport offshore volcanic  
438 islands are volcanic activity, climate and sea-level (Krastel et al., 2001, Quidelleur et al.,  
439 2008). Recent works on the morphology and sedimentary architecture of the Cilaos fan show  
440 that the sedimentary processes involved in the feeding of the Cilaos turbidite systems are  
441 direct feeding by rivers and submarine slope instabilities (Saint-Ange et al., 2011; Sisavath et  
442 al., 2011). The detailed stratigraphy of the Cilaos fan obtained in the present study allows us  
443 to test this assumption over the last climatic cycle.

444

445 *5.2.1 Turbidites in relation to climate and sea-level fluctuations*

446 Offshore La Réunion Island, the two main intervals of turbidite activity coincide with the  
447 transition from glacial lowstand to highstand condition. The first phase of turbidite deposits

448 coincided with lowstand and rising sea-level, at about 137 ka and between 137 and 130 ka,  
449 respectively (Rohling et al., 2009; Fig. 8). The last recurrence of turbidite deposition in the  
450 Cilaos system (unit U3) also coincided with such a sea-level pattern, the turbidite activity is  
451 visible during the LGM lowstand (26 to 19.5 ka, Clark et al., 2009) and continuing until the  
452 next highstand conditions. The intervening period did not show any turbiditic conditions.

453 A link between sea-level change and large scale landsliding is suggested by some authors (e.  
454 g., McMurtry et al., 2004; Quidelleur et al., 2008). Sea-level variations can change the pore  
455 pressure conditions, which are related to the location of the aquifer on top of a hydrothermal  
456 unit (Join et al., 2005) , or influence the submarine and coastal boundary conditions that  
457 control groundwater flow in the volcanic edifice. In his study of factors that could induce  
458 large flank destabilization on shield volcanoes, Iverson (1995) had already concluded to the  
459 minor role played by sea level changes. When the sea-level drops, the mechanical resistance  
460 of the hydrothermal unit decreases as the pressure exerted by the water table at the base of  
461 edifice increases. The mechanical resistance decreases until the rupture threshold is reached,  
462 inducing a rapid lateral sliding of the volcano flank. This link between sea-level change and  
463 large scale landsliding is not observed for the Cilaos fan because no flank collapses have  
464 destabilized the studied area for 1 Ma (Oehler et al., 2008). Moreover, turbidite activity is  
465 visible during lowstand and highstand conditions, suggesting that sea-level variation has little  
466 influence on the development of turbidites in the Cilaos deep-sea fan.

467

468 The lack of palaeoclimatic records from La Réunion Island preclude the direct correlation of  
469 the turbidite activity in the Cilaos Fan with climate changes. An alternative is to examine the  
470 palaeoclimatic reconstructions from southern Africa. Intense debate persists about the  
471 climatic mechanisms governing hydrologic changes in this area (e.g., Schefuß et al., 2012).  
472 However, recent results suggest that mean summer insolation controls the atmospheric

473 convection, with higher insolation leading to higher rainfall (Schefuß et al., 2012). By  
474 considering this orbital forcing over a geological timescale, this implies that glacial-  
475 interglacial transitions in the southern African tropics were characterized by significant  
476 changes in rainfall level, from wet to dry conditions. Such a pattern has been demonstrated for  
477 the last Termination, through the runoff of the Zambezi river (Schefuß et al., 2012), and  
478 corroborates previous rainfall reconstructions from South Africa and Madagascar over the last  
479 150-200 ka (Partridge et al., 1997; Gasse and Van Campo, 2001).

480 Based on a geomorphological approach, Saint-Ange et al. (2011) showed that the Cilaos Fan  
481 is directly connected to the Saint-Etienne river mouth. This implies that river runoff is a major  
482 forcing factor on sediment delivery to the Cilaos Fan, and that a high rainfall period in the  
483 southern African tropics would increase sediment supply to the deep-sea fan. A sediment  
484 delivery process of this type to a deep-depositional system has been demonstrated from short,  
485 mountainous river systems (e.g., Makran margin, Southern California; Bourget et al., 2010;  
486 Covault et al., 2010). Based on the rainfall reconstructions of Partridge et al. (1997) (Fig. 8),  
487 one would expect the turbidite sedimentation in the Cilaos Fan to increase during southern  
488 hemisphere summer insolation maxima. However, no turbiditic activity was recorded in the  
489 Cilaos Fan at the time of glacial rainfall maxima (e.g., ca 90, 70 or 50 ka; Partridge et al.,  
490 1997). Moreover, the turbidite activity off the St Etienne river, centred on Termination II and  
491 I, began at a time of wet (MIS 2) to very wet conditions (MIS 6) in the southern African  
492 tropics and continued during both the climatic transition (i.e., Terminations) and the following  
493 dry conditions (i.e., MIS 5 and MIS 1) (Partridge et al., 1997; Gasse and Van Campo, 2001).

494 To understand the impact of climate on the development of turbidite in the Cilaos fan, it  
495 would be necessary to obtain more accurate data about the climatic variations in La Réunion  
496 Island but, according to current knowledge, the results presented here call into question the  
497 impact of rainfall level alone on sediment delivery to the Cilaos basin.

498

499 *5.2.2 Turbidites in relation to volcanic activity*

500

501 The two main periods of turbidite activity in the Cilaos system coincided with periods of low  
502 effusive volcanic activity at La Réunion. Indeed, the first phase of turbidite activity (unit U1)  
503 can be associated with the low effusive activity identified between 180 and 140 ka at Piton  
504 des Neiges (Kluska, 1997; Salvany et al., 2012). The second period of turbidite activity (Unit  
505 U3) began at the end of the effusive activity of the Piton des Neiges volcano, dated at about  
506 30 ka by Gillot and Nativel (1982). These periods correlate with the major erosional episodes  
507 interpreted by Kluska (1997) and Salvany et al. (2012) (Fig. 10). The decrease of volcanic  
508 production coincided with the erosional formation of the cirques (Kluska, 1997; Salvany et  
509 al., 2012). This strongly suggests that the low effusive activity contributed to increasing the  
510 sediment input to the submarine flank and the deep Cilaos basin surrounding La Réunion  
511 Island. Conversely, the interruption of turbidite activity (between 127 ka and 30 ka) coincided  
512 with a resumption of the effusive and explosive activity of the Piton des Neiges volcano, with  
513 large lava flows that filled the cirques and their drainage valleys (Fig. 10) (Kluska, 1997,  
514 Salvany et al., 2012). In the cirque of Cilaos, the first lava flows related to this new volcanic  
515 event are estimated to have appeared at 130 ka (Kluska, 1997). The filling of the drainage  
516 basin by lava flows probably obstructed the pathways for sediment transfers to the deep  
517 marine environment.

518 In the Canary Islands, for comparison, a clear relationship is observed between the timing of  
519 emplacement of volcanic-rich turbidites and the period of explosive volcanic activity (Alibés  
520 et al., 1999; Frenz et al., 2009). During volcanically active stages, an increase of sediment  
521 transport from the volcanic island is observed, with major flank collapses feeding turbidite  
522 currents (Frenz et al., 2009; Schneider et al., 1998). Schneider et al. (1998) also observed

523 increases of turbidite activity during a non-eruptive period on Gran Canaria, suggesting that  
524 sediments were transported by low-density turbidity currents with some turbidites related to  
525 the dynamics of the fluvial system. Funck and Schmincke (1998) showed that many of the  
526 submarine canyons of the Canary Islands are the continuation of onshore canyons. Mitchell et  
527 al. (2003) and Krastell et al. (2001) concluded that the dominant process feeding these  
528 canyons was hyperpycnal flow.

529 For the Cilaos fan, the occurrence of turbidite activity during periods of low effusive volcanic  
530 activity suggests that the fan was mainly fed by river sediment load. This means that the  
531 turbidite activity occurred when erosional processes dominated, allowing a vast transport of  
532 sediment over the submarine flanks of the volcano. These periods also correspond to phases  
533 of explosive activity of Piton des Neiges, which could also have produced a large amount of  
534 volcanoclastic material during eruption and a rapid transfer of sediments down to the adjacent  
535 slope and basin, in a similar way to what was suggested for the Canary Islands (Schmincke and  
536 Sumita, 1998).

537 As a result, the volcanic activity appears to be a major controlling factor influencing turbidite  
538 development of the Cilaos deep-sea fan.

539

## 540 **6. Conclusions**

541

542 New stratigraphical data on the deep-sea Cilaos sedimentary system allow us to define the  
543 timing of turbidite activity, which appears to have occurred close to the last two climatic  
544 terminations. A first turbidite activity period occurred around 127 ka and a second one started  
545 at 30 ka, which has continued until the present. The two main phases of turbidite activity  
546 coincide with the last two transitions from glacial lowstands to subsequent sea level rises.  
547 Nevertheless, our study demonstrates that sea level change played a minor role in the

548 triggering of turbidites in the Cilaos fan. On the other hand, the synchronicity between intense  
549 turbidite deposition in the Cilaos deep-sea fan and periods of low effusive volcanic activity of  
550 the Piton des Neiges volcano is clearly seen. We suggest that high erosional rates, identified  
551 in the cirques during periods of low effusive activity, would mainly have contributed to  
552 increase the seaward sediment transport. Conversely, the onset of volcanic activity would  
553 have prevented intense erosion in the cirques, with the decrease of gravity deposits in the  
554 Cilaos deep-sea fan resulting from the consequent low sediment transfer by rivers. Compared  
555 with other volcanoclastic systems, explosive events of the Piton des Neiges might have also  
556 contributed to feeding the Cilaos deep-sea fan.

557

## 558 **Acknowledgements**

559

560 The authors thank the crew and scientific teams for the high-quality data recovery during the  
561 2006 ERODER1 cruise aboard the BHO *Beautemps-Beaupré* and the 2008 ERODER 2 cruise  
562 aboard the RV *Meteor*. Seven radiocarbon dates presented in this paper were acquired with  
563 the Artemis program (supported by the CNRS). We are also grateful to Nathalie Labourdette  
564 (Université Pierre & Marie Curie) who ran the oxygen isotope analyses and to Tomasz Goslar  
565 who managed additional radiocarbon dating at the Poznan Radiocarbon Laboratory (Poland).  
566 Financial support was provided by the “Conseil Régional de La Réunion”, by the Institut  
567 Universitaire Européen de la Mer (Brest), and by IFREMER (Project “French Territories –  
568 Indian Ocean”). The authors thank Marie-France Loutre for the insolation data and the two  
569 reviewers Dr. Francky Saint-Ange and Dr. Neil C. Mitchell whose comments and suggestions  
570 contributed to improve the original manuscript.

571

## 572 **References**

573

574

575 Alibés, B., Rothwell, R.G., Canals, M., Weaver, P.P.E., Alonso, B., 1999. Determination of  
576 sediment volumes, accumulation rates and turbidite emplacement frequencies on the  
577 Madeira Abyssal Plain (NE Atlantic): a correlation between seismic and borehole  
578 data. *Marine Geology* 160, 225-250.

579 Andresen, N., Reijmer, J.J.G., Droxler, A.W., 2003. Timing and distribution of calciturbidites  
580 around a deeply submerged carbonate platform in a seismically active setting (Pedro  
581 Bank, Northern Nicaragua Rise, Caribbean Sea). *International Journal of Earth  
582 Sciences* 92, 573-592.

583 Arnaud, N., 2005. Les processus de demantelement des volcans, le cas d'un volcan bouclier  
584 en milieu oceanique : le Piton des Neiges (Ile de La Réunion), Université de La  
585 Réunion, France, 422 pp.

586 Bachelery, P., Chevallier, L., Gratier, J.P., 1983. Structural characteristics of historical  
587 eruptions of the Piton de la Fournaise (Reunion Island). *Comptes Rendus De  
588 l'Academie Des Sciences Serie II* 296 (17), 1345-1350.

589 Berger, A.L., 1978: Long-Term Variations of Daily Insolation and Quaternary Climatic  
590 Changes. *Journal of the Atmospheric Sciences*, **35**, 2362–2367.

591 Berggren, W.A. et al., 1995. Late Neogene chronology: New perspectives in high-resolution  
592 stratigraphy. *Geological Society of America Bulletin* 107 (11), 1272-1287.

593 Bonneville, A., Barriot, J.P., Bayer, R., 1988. Evidence from geoid data of a hotspot origin for  
594 the southern Mascarene Plateau and Mascarene Islands (Indian Ocean). *Journal of  
595 geophysical research* 93 (B5), 4199-4212.

596 Bouma, A.H., 1962. Sedimentology of some flysh deposits: a graphic approach to facies  
597 interpretation. Elsevier, Amsterdam, 168 pp.

598 Bourget, J., Zaragosi, S., Mulder, T., Schneider, J.-L., Garlan, T., Van Toer, A., Mas, V.,  
599 Ellouz-Zimmermann, N., 2010. Hyperpycnal-fed turbidite lobe architecture and recent  
600 sedimentary processes: A case study from the Al Batha turbidite system, Oman  
601 margin. *Sedimentary Geology* 229, 144-159.

602 Bret, L., Fevre, Y., Join, J.L., Robineau, B., Bachelery, P., 2003. Deposits related to  
603 degradation processes on Piton des Neiges volcano (Reunion Island): overview and  
604 geological hazard. *Journal of Volcanology and Geothermal Research* 123 (1-2), 25-41.

605 Clark, P.U. et al., 2009. The last glacial maximum. *Science* 325, 710-714.

606 Covault, J.A., Normark, W.R., Romans, B.W., Graham, S.A., 2007. Highstand fans in the  
607 California borderland: The overlooked deep-water depositional systems. *Geology* 35,  
608 783-786.

609 Covault, J.A., Graham, S.A., 2010. Submarine fans at all sea-level stands: Tectono-  
610 morphologic and climatic controls on terrigenous sediment delivery to the deep sea.  
611 *Geology* 38 (10), 939-942.

612 De Voogd, B. et al., 1999. Vertical movements and material transport during hotspot activity:  
613 seismic reflection profiling offshore La Reunion. *Journal of Geophysical Research-  
614 Solid Earth* 104, 2855–2874.

615 Deniel, C., Kieffer, G., Lecointre, J., 1992. New Th-230-U-238 and C-14 age determinations  
616 from Piton des Neiges volcano, Reunion-A revised chronology for the Differentiated  
617 Series *Journal of Volcanology and Geothermal Research* 51 (3), 253-267.

618 Divakar Naidu, P., Malmgren, B.A., Bornmalm, L., 1993. Quaternary history of calcium  
619 carbonate fluctuations in the western equatorial Indian Ocean (Somali Basin).  
620 *Palaeogeography, Palaeoclimatology, Palaeoecology* 103, 21-30.

621 Droxler, A.W., Schlager, W., 1985. Glacial versus interglacial sedimentation rates and  
622 turbidite frequency in the Bahamas. *Geology* 13 (11), 799-802.



623 Ducassou, E. et al., 2010. Evolution of the Nile deep-sea turbidite system during the Late  
624 Quaternary: influence of climate change on fan sedimentation. *Sedimentology* 56,  
625 2061-2090.

626 Duncan, R.A., Backman, J., Peterson, L., 1989. Reunion hotspot activity through tertiary  
627 time: initial results from the Ocean Drilling Program, leg 115. *Journal of Volcanology*  
628 and *Geothermal Research* 4, 193-198.

629

630 Fèvre, Y., 2005. Mécanismes et vitesses d'érosion à l'échelle géologique sur une île  
631 volcanique jeune à relief élevé - La Réunion (Océan Indien). Université de la Réunion,  
632 France, 217 pp.

633 Frenz, M. et al., 2009. Provenance and pathways of late Quaternary turbidites in the deep-  
634 water Agadir Basin, northwest African margin. *International Journal of Earth Sciences*  
635 98 (4), 721-733.

636 Fretzdorff, S., Paterne, M., Stoffers, P., Ivanova, E., 2000. Explosive activity of the Reunion  
637 Island volcanoes through the past 260,000 years as recorded in deep-sea sediments.  
638 *Bulletin of Volcanology* 62 (4-5), 266-277.

639 Funck, T., Schmincke, H.U., 1998. Growth and destruction of Gran Canaria deduced from  
640 seismic reflection and bathymetric data. *Journal of Geophysical Research* 103 (B7),  
641 393-407.

642 Gasse F, Van Campo E. 2001. Late Quaternary environmental changes from a pollen and  
643 diatom record in the southern tropics (Lake Tritrivakely, Madagascar).  
644 *Palaeogeography, Palaeoclimatology, Palaeoecology* 167: 287-308

645 Gillot, P.Y., Nativel, P., 1982. K-Ar chronology of the ultimate activity of Piton des Neiges  
646 volcano, Reunion Island, Indian Ocean. *J. Volcano. Geotherm. Res.* 13, 131-146.

647 Gillot, P.Y., Nativel, P., 1989. Eruptive history of the Piton de la Fournaise volcano, Réunion  
648 Island, Indian Ocean. *Journal of Volcanology and Geothermal Research* 36 (1-3), 53-  
649 65.

650 Harris, P.D., Branney, M.J., Storey, M., 2011. Large eruption-triggered ocean-island landslide  
651 at Tenerife: Onshore record and long-term effects on hazardous pyroclastic dispersal.  
652 *Geology* 39, 951-954.

653 Iverson, R.M., 1995. Can magma-injection and groundwater forces cause massive landslides  
654 on Hawaiian volcanoes? *Journal of Volcanology Geotherm. Res.* 66, 295–308.

655 Join, J.-L., Folio, J.-L., Robineau, B., 2005. Aquifers and groundwater within active shield  
656 volcanoes. Evolution of conceptual models in the Piton de la Fournaise volcano.  
657 *Journal of Volcanology and Geothermal Research* 147, 187-201.

658 Jorry, S.J., Droxler, A.W., Francis, J.M., 2010. Deepwater carbonate deposition in response to  
659 re-flooding of carbonate bank and atoll-tops at glacial terminations. *Quaternary*  
660 *Science Reviews* 29, 2010-2026.

661 Jorry, S.J. et al., 2008. Bundled turbidite deposition in the central Pandora Trough (Gulf of  
662 Papua) since Last Glacial Maximum: Linking sediment nature and accumulation to  
663 sea level fluctuations at millennial timescale. *Journal of geophysical research* 113  
664 (F01S19).

665 Jorry, S.J., Jégou, I., Emmanuel, L., Silva Jacinto, R., Savoye, B., 2011. Turbiditic levee  
666 deposition in response to climate changes: The Var Sedimentary Ridge (Ligurian Sea).  
667 *Marine Geology* 279 (1-4), 148-161.

668 Kieffer, G., 1990. Grand traits morphologiques de l'île de la Réunion (Océan Indien). In: J.F.  
669 Lénat (Ed.), *Le Volcanisme de la Réunion - Monographie*, pp. 75-114.

670 Kluska, J.M., 1997. Evolution magmatique et morpho-structurale du Piton des Neiges au  
671 cours des derniers 500 000 ans, Paris XI.

672 Krastel, S., Schmincke, H.U., Jacobs, C.L., 2001. Formation of submarine canyons on the  
673 flanks of the Canary Islands. *Geo-Marine Letters* 20 (3), 160-167.

674 Lenat, J.F. et al., 2009. Age and nature of deposits on the submarine flanks of Piton de la  
675 Fournaise (Reunion Island). *Journal of Volcanology and Geothermal Research* 184 (1-  
676 2), 199-207.

677 Lenat, J.F. and Labazuy, P., 1990. Morphologies et structures sous-marines de La Réunion. In  
678 “Le volcanisme de la Réunion, monographie”, J-F Lénat Ed., pp379, 43-74.

679 Lisiecki, L.E., Raymo, M.E., 2005. A Pliocene-Pleistocene stack of 57 globally distributed  
680 benthic  $\delta^{18}\text{O}$  records. *Paleoceanography* 20 (PA1003), 1-17.

681 Longpré, M.-A., Chadwick, J.P., Wijbrans, J., Iping, R., 2011. Age of the El Golfo debris  
682 avalanche, El Hierro (Canary Islands): New constraints from laser and furnace  
683  $^{40}\text{Ar}/^{39}\text{Ar}$  dating. *Journal of Volcanology and Geothermal Research* 203, 76-80.

684 Louvat, P., Allegre, C.J., 1997. Present denudation rates on the island of Reunion determined  
685 by river geochemistry: Basalt weathering and mass budget between chemical and  
686 mechanical erosions. *Geochimica et Cosmochimica Acta* 61 (17), 3645-3669.

687 McDougall, I., 1971. The geochronology and evolution of the young volcanic island of  
688 Réunion, Indian Ocean. *Geochimica et Cosmochimica Acta* 35 (3), 261-288.

689 McMurtry, G.M., Watts, P., Fryer, G.J., Smith, J.R., Imamura, F., 2004. Giant landslides,  
690 mega-tsunamis, and paleo-sea level in the Hawaiian Islands. *Marine Geology* 203 (3-  
691 4), 219-233.

692 Michon, L., Saint-Ange, F., 2008. Morphology of Piton de la Fournaise basaltic shield  
693 volcano (La Reunion Island): Characterization and implication in the volcano  
694 evolution. *Journal of Geophysical Research-Solid Earth* 113, B03203.

695 Migeon, S., Weber, O., Faugères, J.-C., Saint-Paul, J., 1999. SCOPIX: A new X-ray imaging  
696 system for core analysis. *Geo-Marine Letters* 18, 251-255.

697 Mitchell, N.C., Dade, W.B., Masson, D.G., 2003. Erosion of the submarine flanks of the  
698 Canary Islands. *Journal of Geophysical Research-Earth Surface* 108, F1-6002.

699 Morgan, W.J., 1981. Hot spot tracks and the opening of the Atlantic and Indian Oceans. In: C.  
700 Emiliani (Ed.), *The Sea*. Wiley Interscience, New York, pp. 443-487.

701 Oehler, J.-F., Lénat, J.-F., Labazuy, P., 2008. Growth and collapse of the Reunion Island  
702 volcanoes. *Bulletin of Volcanology* 70, 717–742.

703 Oehler, J.F., de Vries, B.V., Labazuy, P., 2005. Landslides and spreading of oceanic hot-spot  
704 and arc shield volcanoes on Low Strength Layers (LSLs): an analogue modeling  
705 approach. *Journal of Volcanology and Geothermal Research* 144 (1-4), 169-189.

706 Oehler, J.F., Labazuy, P., Lenat, J.F., 2004. Recurrence of major flank landslides during the  
707 last 2-Ma-history of Reunion Island. *Bulletin of Volcanology* 66, 585–598.

708 Ollier, G., Cochonat, P., Lenat, J.F., Labazuy, P., 1998. Deep-sea volcanoclastic sedimentary  
709 systems: an example from La Fournaise volcano, Reunion Island, Indian Ocean.  
710 *Sedimentology* 45 (2), 293-330.

711 Ollier, C.D., Terry, J.P., 1999. Volcanic geomorphology of northern Viti Levu, Fiji.  
712 *Australian Journal of Earth Sciences* 46, 515-522

713 Patridge, T.C., Demenocal, P.B., Lorentz, S.A., Paiker, M.J., Vogel, J.C., 1997. Orbital  
714 forcing of climate over South Africa: A 200,000-year rainfall record from the Pretoria  
715 Saltpan. *Quaternary Science Reviews* 16, 1125-1133.

716 Peltier, A., Bachelery, P., Staudacher, T., 2009. Magma transport and storage at Piton de La  
717 Fournaise (La Reunion) between 1972 and 2007: A review of geophysical and  
718 geochemical data. *Journal of Volcanology and Geothermal Research* 184 (1-2), 93-  
719 108.

720 Peltier, A. et al., 2008. Cyclic magma storages and transfers at Piton de La Fournaise volcano  
721 (La Reunion hotspot) inferred from deformation and geochemical data. *Earth and*  
722 *Planetary Science Letters* 270 (3-4), 180-188.

723 Quidelleur, X., Hildenbrand, A., Samper, A., 2008. Causal link between Quaternary  
724 paleoclimatic changes and volcanic islands evolution. *Geophysical Research Letters*  
725 35, L02303.

726 Quidelleur, X., Holt, J.W., Salvany, T., Bouquerel, H., 2010. New K-Ar ages from La  
727 Montagne massif, Reunion Island (Indian Ocean), supporting two geomagnetic events  
728 in the time period 2,2-2,0 Ma. *Geophysical Journal International* 182 (2), 699-710.

729 Rad, S.D., Allegre, C.J., Louvat, P., 2007. Hidden erosion on volcanic islands. *Earth and*  
730 *Planetary Science Letters* 262, 109-124.

731 Reimer, P.J. et al., 2009. Intcal09 and Marine09 radiocarbon age calibration curves, 0–50,000  
732 years cal BP. *Radiocarbon* 51 (4), 1111-1150.

733 Rodriguez-Gonzales, A. et al., 2009. The Holocene volcanic history of Gran Canaria island:  
734 implications for volcanic hazards. *Journal of Quaternary Science* 24 (7), 697-709.

735 Rohling, E.J. et al., 2009. Antarctic temperature and global sea level closely coupled over the  
736 past five glacial cycles. *Nature Geoscience* 2, 500-504.

737 Saint-Ange, F. et al., 2011. A volcanoclastic deep-sea fan off La Réunion Island (Indian  
738 Ocean): gradualism versus catastrophism. *Geology* 39, 271-274.

739 Salvany, T., Lahitte, P., Nativel, P., Gillot, P.-Y., 2012. Geomorphic evolution of the Piton  
740 des Neiges volcano (Réunion Island, Indian Ocean): Competition between volcanic  
741 construction and erosion since 1.4 Ma. *Geomorphology*,  
742 doi:10.1016/j.geomorph.2011.06.009.

743 Schefuß, E., Kuhlmann, H., Mollenhauer, G., Prange, M., Pätzold, J., 2011. Forcing of wet  
744 phases in southeast Africa over the past 17, 000 years. *Nature* 480, 509-512.

745 Schlager, W., Reijmer, J.J.G., Droxler, A.W., 1994. Highstand shedding of carbonate  
746 platforms. *Journal of sedimentary Research* B64 (3), 270-281.

747 Schmincke, H.U., Sumita, M., 1998. Volcanic evolution of Gran Canaria reconstructed from  
748 apron sediments: synthesis of VICAP Project Drilling. In: P.P.E. Weaver, Schmincke,  
749 H.-U., et al., eds., *Proc. ODP, Sci. Results, 157: College Station, TX (Ocean Drilling  
750 Program) (Ed.)*, pp. 443-469.

751 Schneider, J.L., Brunner, C.A., Kuttner, S., 1998. Epiclastic sedimentation during the upper  
752 Miocene-lower Pliocene volcanic hiatus of Gran Canaria: evidence from sites 953 and  
753 954. In: P.P.E. Weaver, Schmincke, H.-U., et al., eds., *Proc. ODP, Sci. Results, 157:  
754 College Station, TX (Ocean Drilling Program) (Ed.)*, pp. 293-313.

755 Sisavath, E. et al., 2011. Morphology and sedimentary architecture of a modern volcanoclastic  
756 turbidite system: The Cilaos fan, offshore La Réunion Island. *Marine Geology*  
757 doi:10.1016/j.margeo.2011.06.011.

758 Smietana, M., Bachèlery, P., Hémond, C., 2010. Heterogeneity in the Mantle Source of La  
759 Réunion Island, *Goldschmidt 2010. Geochimica et Cosmochimica acta* 74 (12 Suppl.  
760 1): A972.

761 Société Grenobloise d'Etudes et d'Application Hydrauliques (SOGREAH), 1998. Etude des  
762 risques hydrauliques sur la Rivière Saint-Etienne. report 554509 R1. 24 pp.

763 Stieltjes, L., Moutou, P., 1988. A statistical and probabilistic study of the historic activity of  
764 Piton de la Fournaise, Reunion Island, Indian Ocean. *Journal of volcanology and  
765 geothermal Research* 36, 67-86.

766 Thompson, P.R., Be, A.W.H., Duplessy, J.-C., Shackleton, N.J., 1979. Disappearance of pink-  
767 pigmented *Globigerinoides ruber* at 120,000 yr BP in the Indian and Pacific Oceans.  
768 *Nature* 280 (5723), 554-558.

769 Toucanne, S. et al., 2008. Activity of the turbidite levees of the Celtic-Armorican margin  
770 (Bay of Biscay) during the last 30,000 years: Imprints of the last European  
771 deglaciation and Heinrich events. *Marine Geology* 247, 84-103.

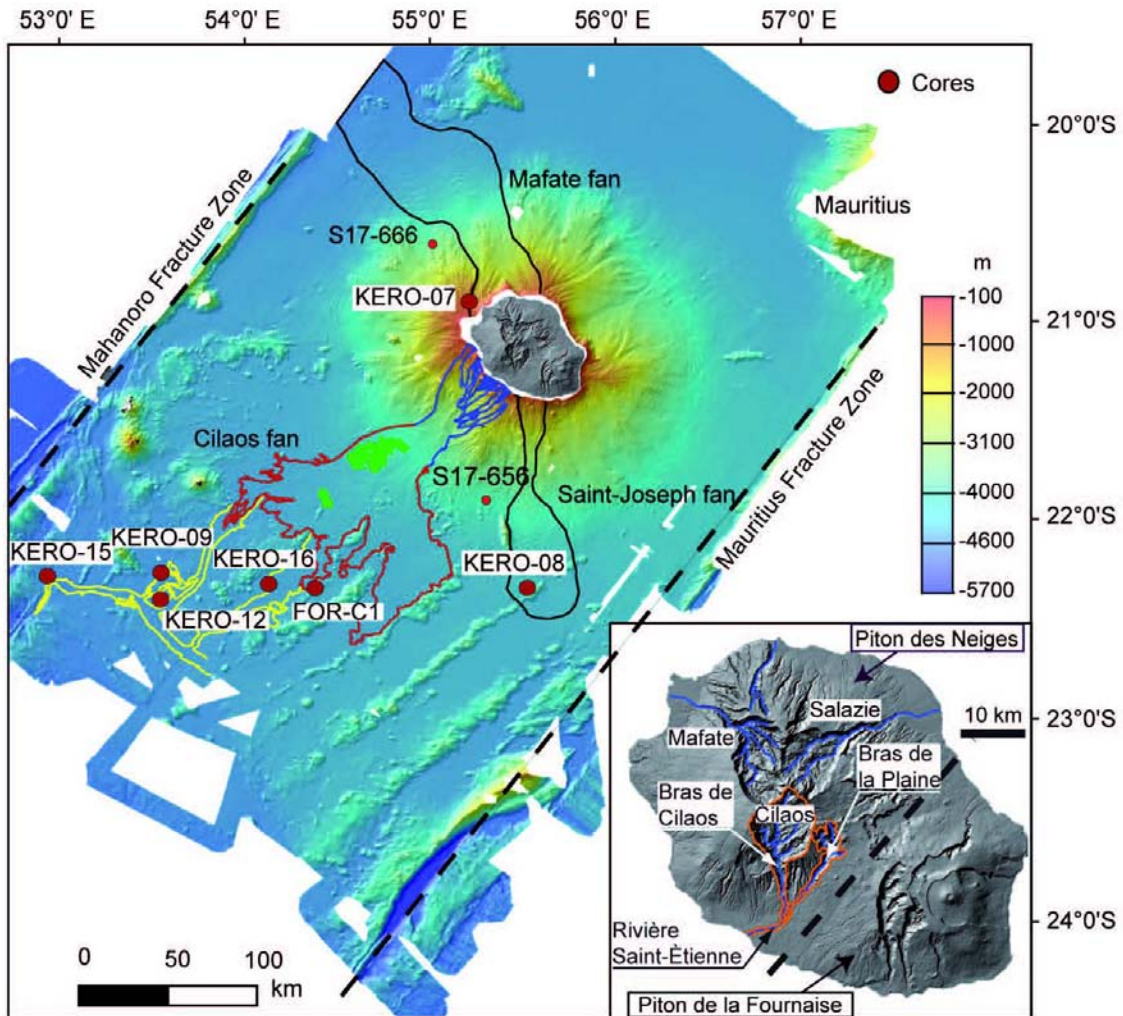
772 Toucanne, S., Zaragosi, S., Bourillet J.F., Dennielou, B., Jorry, S.J., Jouet, G., Cremer, M.,  
773 2012. External controls on turbidite sedimentation on the glacially-influenced  
774 Armorican margin (Bay of Biscay, western European margin). *Marine Geology* 303,  
775 137-153.

776 Upton, B.G.J., Wadsworth, W.J., 1965. The basalt of Réunion Island, Indian Ocean. *Bulletin*  
777 *of volcanology* 29, 7-23.

778

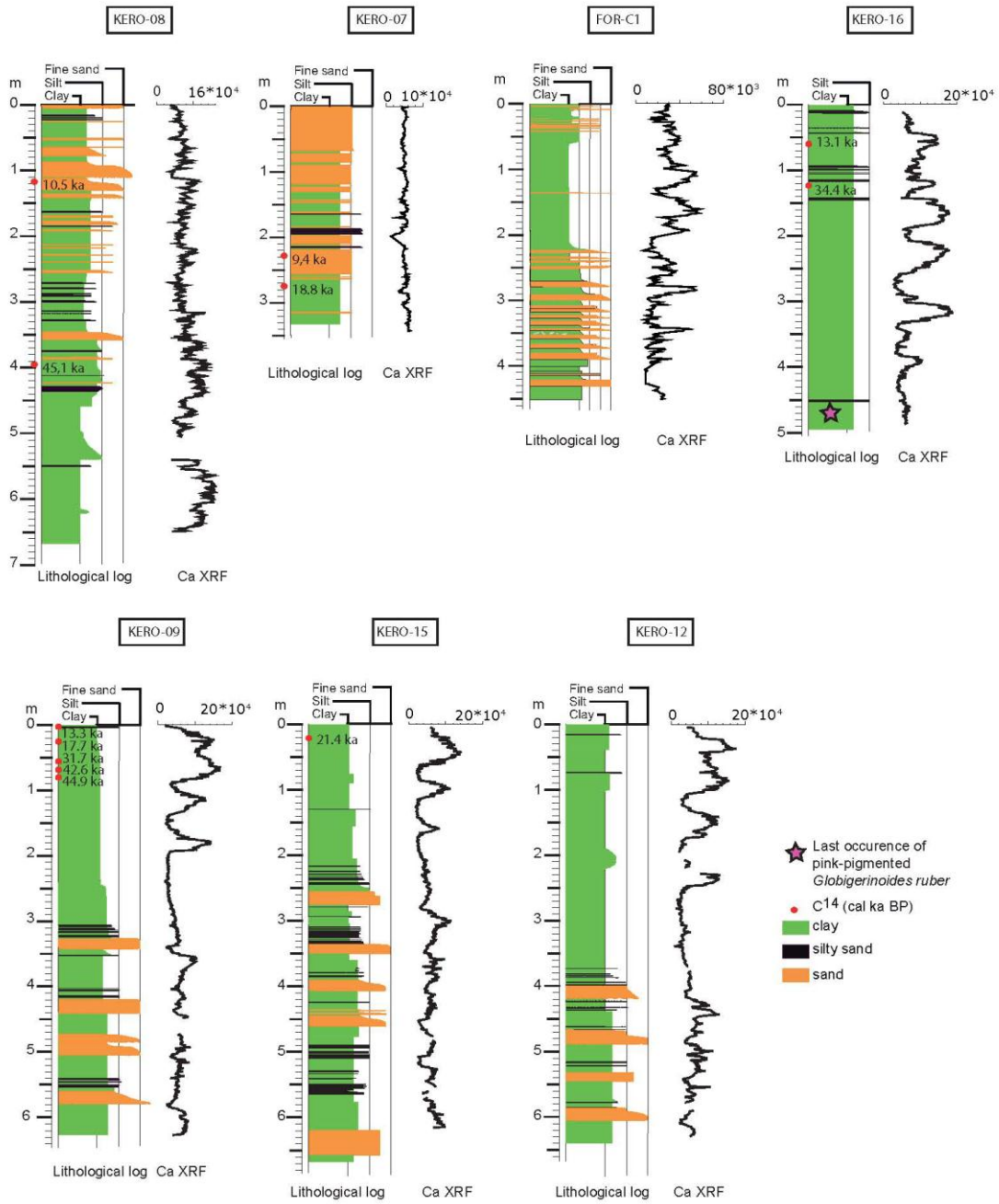
779

780 **Figure captions**



781  
 782 Fig. 1: Interpreted swath bathymetry image of the abyssal plain around La Réunion Island,  
 783 compiled from the ERODER and FOREVER surveys. Red filled dots correspond to sediment  
 784 cores presented in this paper. For the Cilaos fan, canyons are outlined in blue; the proximal  
 785 fan in red and the distal part in yellow. Overview of the main geological structures of La  
 786 Réunion Island (insert). The dashed line represents the separation between the two main  
 787 volcanic edifices. The blue lines correspond to the main rivers draining the cirques. The  
 788 orange lines delimit the main rivers feeding the Saint-Etienne river.



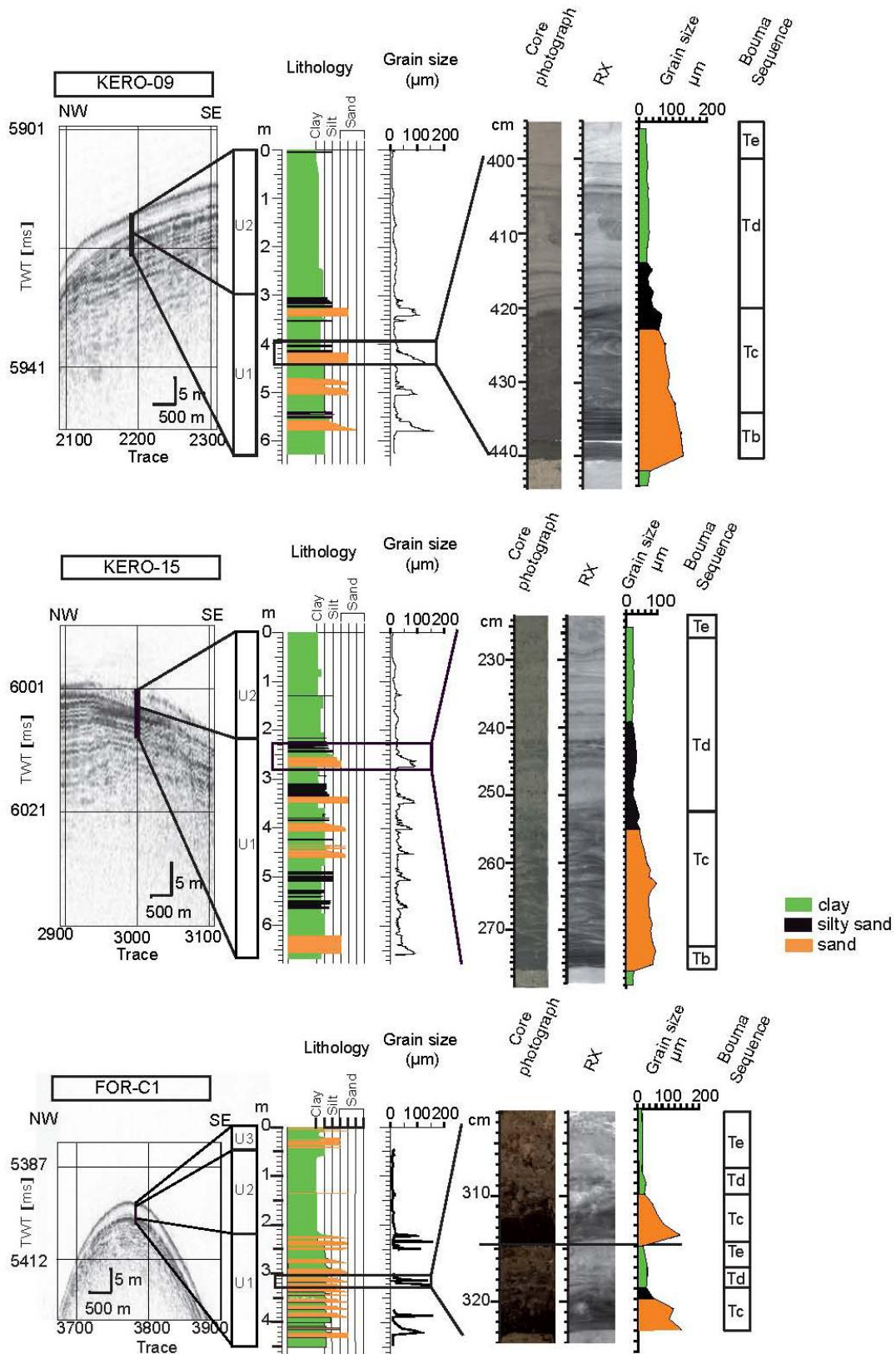


789

790

791 Fig. 2: Lithological logs, fluctuations of Calcium XRF, and AMS <sup>14</sup>C dates (cal ka BP) of

792 cores KERO-07, KERO-08, KERO-09, KERO-12, KERO-15, KERO-16 and FOR-C 1.

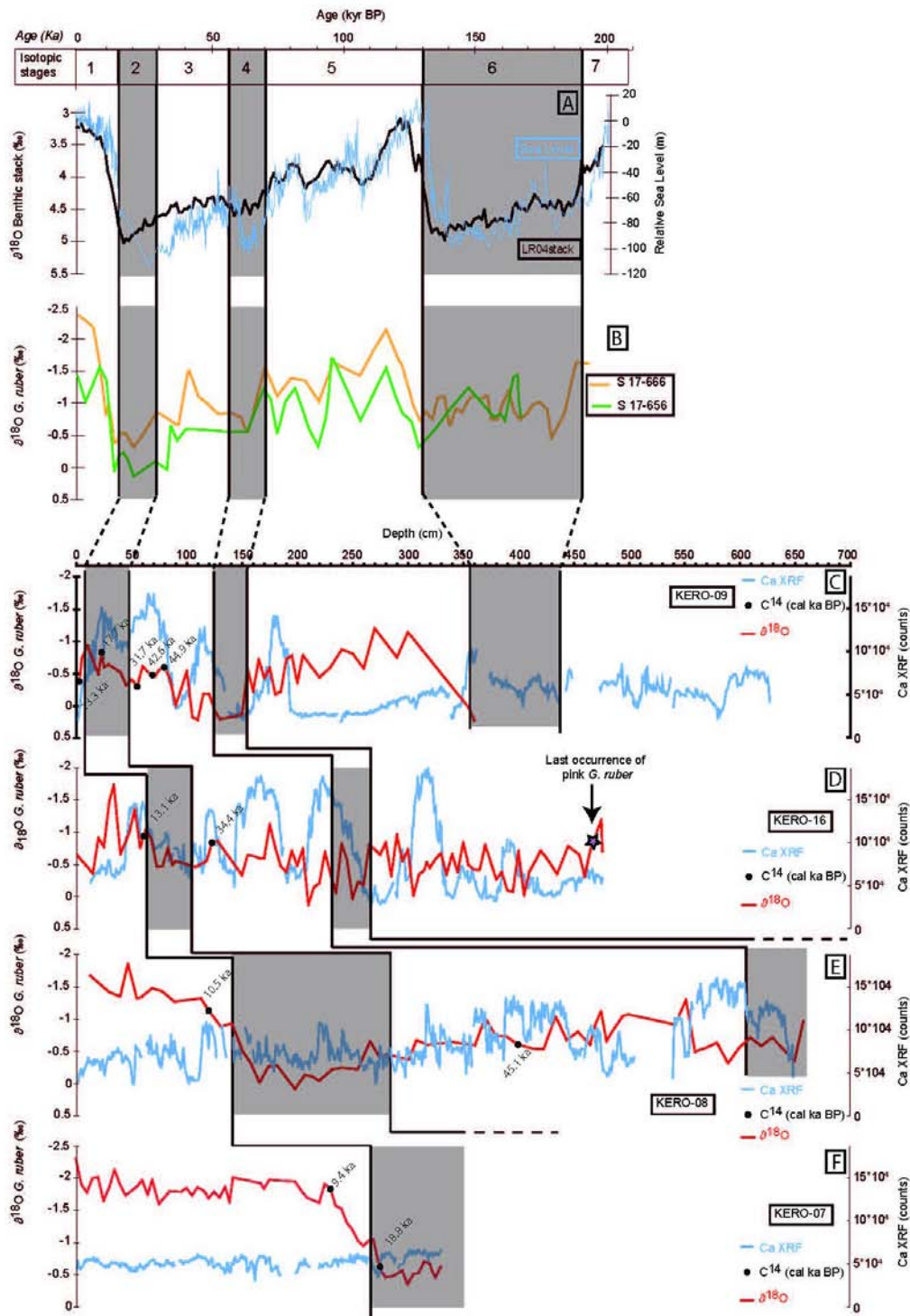


793

794

795 Fig. 3: Lithological log correlated with the corresponding echosounder profile, grain size

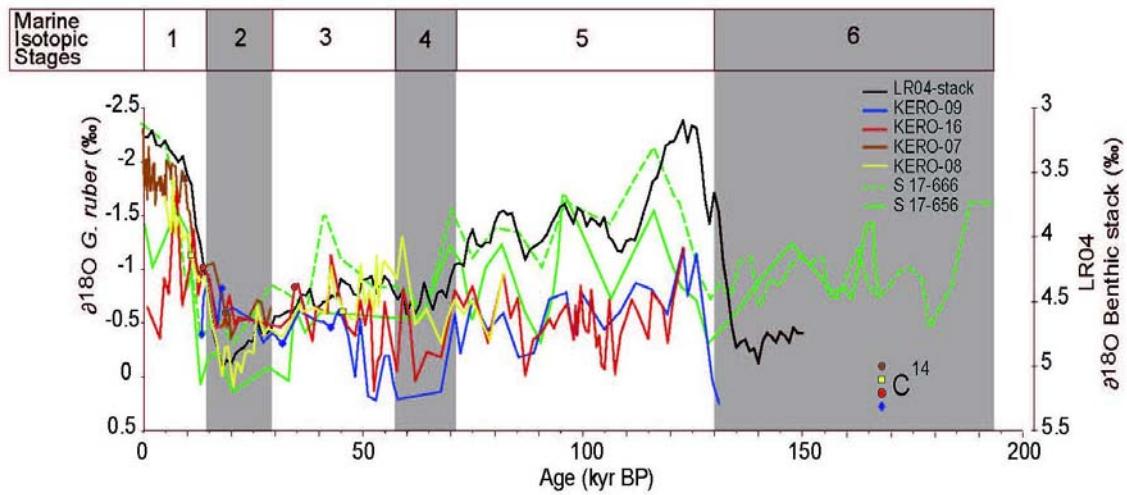
796 curve and X-ray image of cores KERO-09, KERO-15 and FOR-C .



797

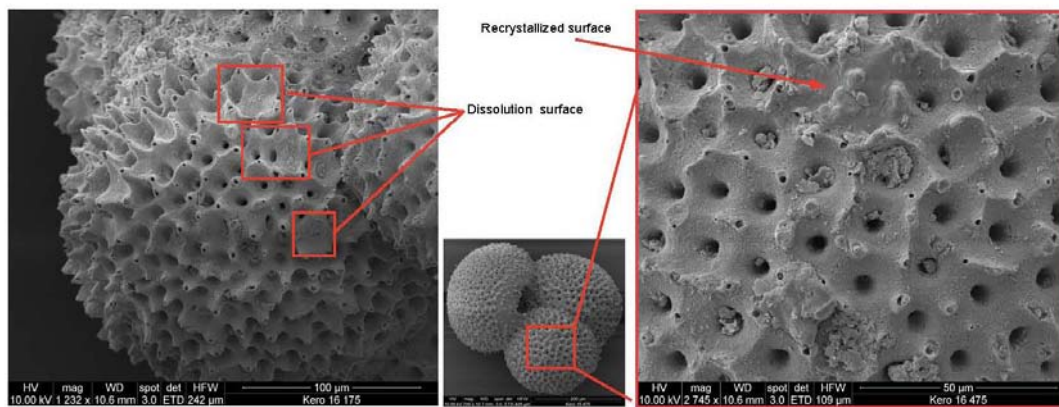
798 Fig. 4: A: LR04  $\delta^{18}\text{O}$  benthic stack from Lisiecki and Raymo (2005). B: *G. ruber*  $\delta^{18}\text{O}$  of  
 799 cores S17-666 and S17-656 (Fretzdorff et al., 2000), locations shown on figure 1. C: *G. ruber*  
 800  $\delta^{18}\text{O}$  and Ca XRF of core KERO-09. D: *G. ruber*  $\delta^{18}\text{O}$  and Ca XRF of core KERO-16. E: *G.*  
 801 *ruber*  $\delta^{18}\text{O}$  and Ca XRF of core KERO-08. F: *G. ruber*  $\delta^{18}\text{O}$  and Ca XRF of core KERO-07.





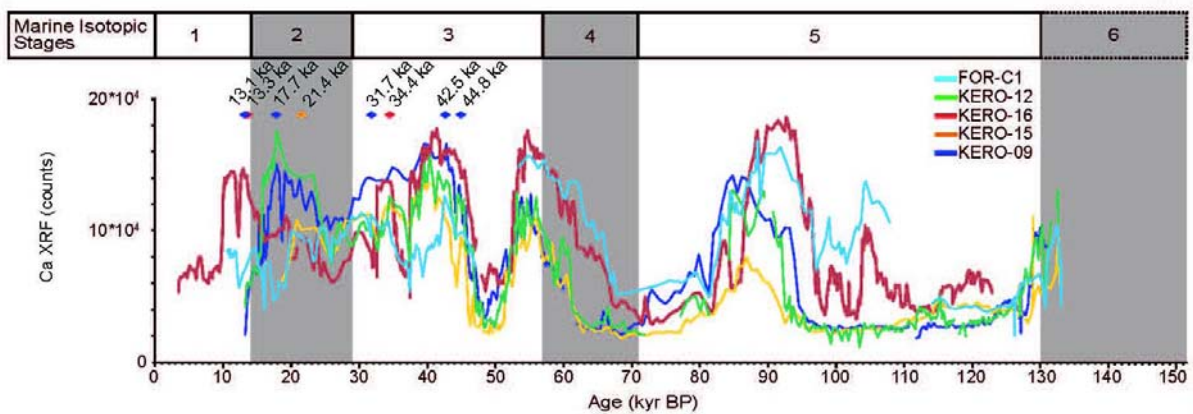
802

803 Fig. 5:  $\delta^{18}\text{O}$  curves of cores KERO-07, KERO-08, KERO-09 and KERO-16 compared with  
 804 the LR04-stack curve of Lisiecki and Raymo (2005).



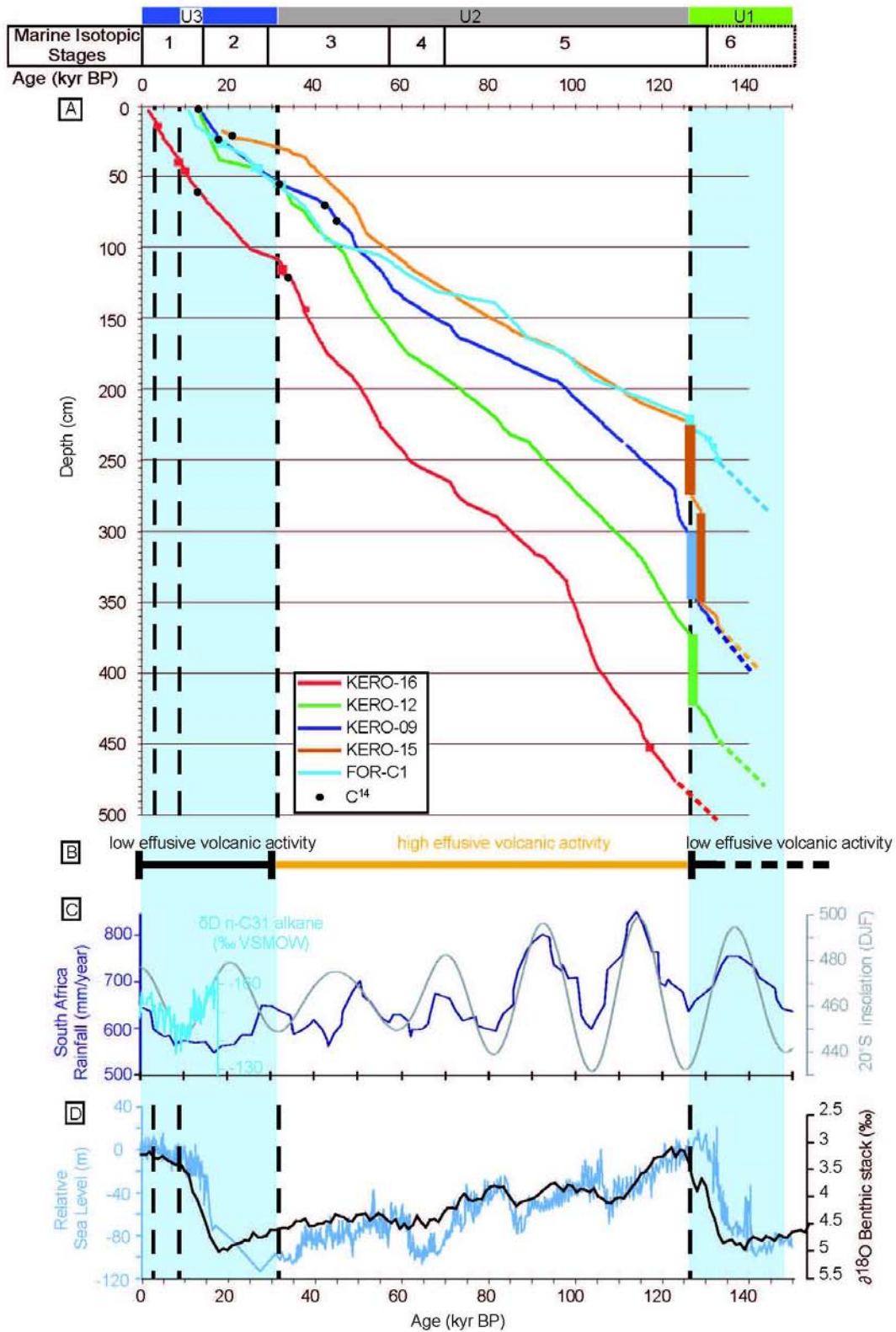
805

806 Fig. 6: SEM microphotographs of *G. ruber* from core KERO-16. Recrystallization and  
 807 dissolution surfaces are indicated on test surfaces.



808

809 Fig. 7: Fluctuations of Calcium XRF for all the studied cores in the Cilaos deep-sea fan.



810

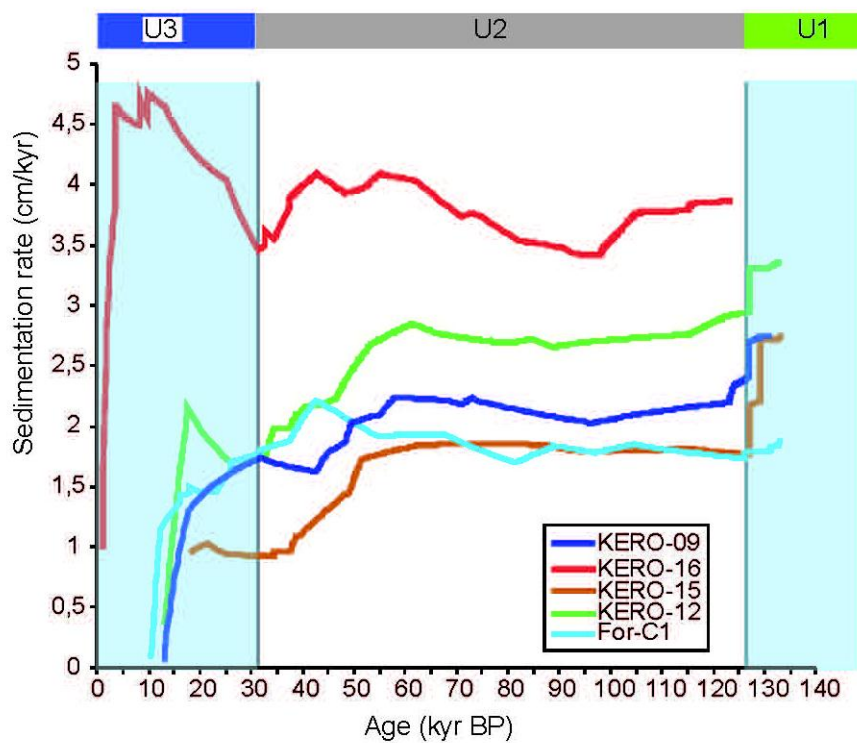
811 Fig. 8: Timing of turbidite deposition in the Cilaos deep-sea fan. Blue areas indicate periods

812 of major turbidite activity. The black dotted lines show the location of main turbidites. A)

813 Age/depth model of the five cores KERO-09, KERO-12, KERO-15, KERO-16 and FOR-C1,

814 showing the location of turbidite beds in each core (turbidite beds are represented by  
 815 rectangles along each age/depth curves; their vertical size is proportional to the turbidite  
 816 thickness along the depth axis). Black dots show AMS  $^{14}\text{C}$  dates. B) Major volcanic episodes  
 817 of Piton des Neiges during the Late Quaternary. Dataset from Kluska (1997), Salvany et al.  
 818 (2012). C) Hydrogen isotope compositions of the n-C31 alkane in GeoB9307-3, reflecting  
 819 rainfall changes in the Zambezi catchment (Schefuß et al., 2012), Pretoria rainfall time series  
 820 from Patridge et al. (1997) and insolation curve from Berger (1978). D) Red Sea sea level  
 821 curve from core GeoTü-KL09 (Rohling et al., 2009) and LR04-stack curve of Lisiecki and  
 822 Raymo (2005).

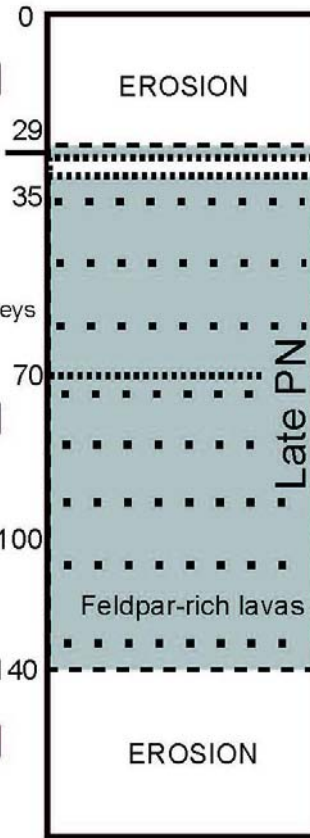
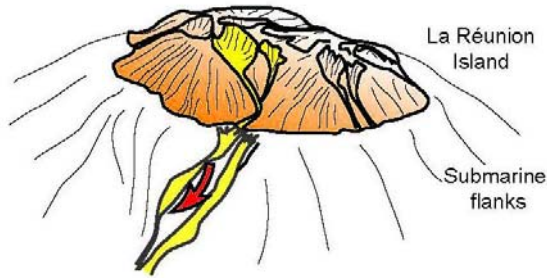
823



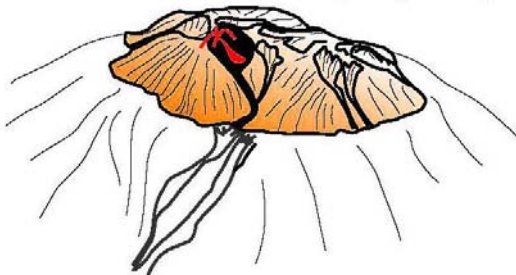
824

825 Fig. 9: Sedimentation rate of the five cores of the Cilaos fan plotted versus time.

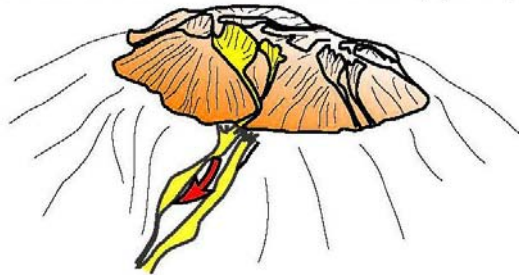
Since 30 ka: Erosion and turbidite activity (U3 deposition)



127-30 ka: Effusive volcanic activity filling the cirque and fluvial valleys



Before 127 ka: Erosion and turbidite activity (U1 deposition)



826

827 Fig. 10: Schematic representation of the transport of sediments on the Cilaos deep-sea fan and  
828 volcano-stratigraphic units of Piton des Neiges (modified from Salvany et al., 2012).

829

Cruises	Cores	Lat (S)	Long (E)	Water Depth (m)	Location	Length (m)
FOREVER	FOR-C1	S22°20.95	E54°23.33	4074	Sedimentary ridge, Central Cilaos Fan	4.51
ERODER1	KERO-07	S20°53.59	E55°12.19	791	Levee, Mafate fan	3.40
ERODER 2	KERO-08	S22°20.89	E 55°31.12	4126	Distal part of Saint-Joseph fan	6.59
ERODER 2	KERO-09	S22°16.347	E53°33.060	4460	Levee, Occ. Cilaos Fan	6.27
ERODER 2	KERO-12	S22°23.550	E53°32.752	4461	Levee, Occ. Cilaos Fan	6.40
ERODER 2	KERO-15	S22°17.39	E52°56.10	4529	Distal levee, Occ. Cilaos Fan	6.68
ERODER 2	KERO-16	S22°19.51	E54°07.78	4340	Levee, Central Cilaos Fan	4.95

831

832 Table 1 : Location, bathymetry and length of the studied cores

833



834

Laboratory number	Core	Depth <u>(cm bsf)</u>	AMS 14C age (yr)	AMS 14C age (-400yr)	Error yr	Calendar Age <u>(cal yr BP)</u>
Poz-35177	KERO-09	3	11 840	11 440	60	13 302
Poz-35178	KERO-09	23	14 980	14 580	70	17 739
Poz-35179	KERO-09	55	28 000	27 600	240	31 723
Poz-35180	KERO-09	69	38 500	38 100	600	42 587
Poz-35181	KERO-09	80	41700	41 300	1000	44 883
SacA 24240	KERO-08	118-119	9680	9280	40	10 543
SacA 24241	KERO-08	395-396	42 060	41 660	690	45 133
SacA 24239	KERO-07	229-230	8755	8355	40	9436
SacA 21880	KERO-07	274.5	16 110	15 710	50	18 834
SacA 21881	KERO-15	21.5	18 390	17 990	60	21 443
SacA 21882	KERO-16	60.5	11 610	11 210	35	13 118
SacA 21883	KERO-16	122.5	29 660	29 260	160	34 422

835

836

837 Table 2 : Radiocarbon dates from cores KERO-07, KERO-08, KERO-09, KERO-15 and  
838 KERO-16

839

Sample	Depth (cm bsf)	Sedimentary Facies	Observation
KERO-09-65	65	Layer of light brown clay, located in the upper part of the core	<i>Emiliana huxleyi</i> abundant (<75-90 Ka)
KERO-09-115	115	Layer of light brown clay,	Abundant, good preservation, <i>Pseudoemiliana lacunosa</i> being absent (<460 ka) and contains <i>Emiliana huxleyi</i> (<260 ka)
KERO-09-117	117	Layer of light brown clay	Abundant, good preservation, <i>Pseudoemiliana lacunosa</i> being absent (<460 ka) and contains <i>Emiliana huxleyi</i> (<260 ka)
KERO-09-361	361	Layer of brown clay, located between two sandy layers	Abundant, good preservation, <i>Pseudoemiliana lacunosa</i> being absent (<460 ka) and contains <i>Emiliana huxleyi</i> (<260 ka). Reworked nannofossils were noted
KERO-09-608	608	Layer of brown clay, located in the lower part of the core	Abundant, poor preservation. <i>Gephyrocapsa spp cf caribbeanica</i> dominant. Two specimens of <i>Pseudoemiliana lacunosa</i> suggest age <460ka.

841

842

843

844

845

Table 3 : Calcareous nannofossil data of core KERO-09. Age from Berggren et al. (1995).